1-6-2004

Oxygen Vacancy Ordering and Magnetism in the Rare Earth Stabilised Perovskite Form of “SrCO3-d

M. James
ANSTO, Australia

D. Cassidy
ANSTO, Australia

K. F. Wilson
Australian National University

J. Horvat
University of Wollongong, jhorvat@uow.edu.au

R. L. Withers
Australian National University

Oxygen Vacancy Ordering and Magnetism in the Rare Earth Stabilised Perovskite Form of "$SrCO_{3-\delta}$".

M. James,[a†] D. Cassidy,[b] K. F. Wilson,[c] J. Horvat[e] and R. L. Withers.[e]

[a]*Bragg Institute, Australian Nuclear Science and Technology Organisation, PMB 1, Menai NSW 2234, Australia.*

[b]*Materials and Engineering Sciences, Australian Nuclear Science and Technology Organisation, PMB 1, Menai NSW 2234, Australia.*

[c]*Department of Physics, Australian National University, Canberra, ACT 0200, Australia.*

[d]*Institute for Superconducting and Electronic Materials, University of Wollongong, NSW 2522, Australia.*

[e]*Research School of Chemistry, Australian National University, Canberra, ACT 0200, Australia.*

[†] Author to whom correspondence should be addressed.

Address for Manuscript Correspondence

Dr Michael James
The Bragg Institute,
Building 58,
ANSTO,
PMB 1,
Menai NSW 2234
Australia.

Email: mja@ansto.gov.au
Phone: +61-2-9717-9299
Fax: +61-2-9717-3606

Abstract

We have demonstrated that $SrCoO_{3-\delta}$ can be stabilised into phase pure perovskite forms by the introduction of small amounts ~5% of certain rare earth ions (Sm^{3+} - Yb^{3+}). At the same doping levels, La^{3+} and Pr^{3+} crystallise with the same isostructural trigonal structure as $SrCoO_{3-d}$; while the Nd^{3+} composition shows a mixture of both structure types. Powder X-ray diffraction showed only a simple cubic perovskite structure, however a combination of electron and neutron diffraction has revealed a tetragonal (*P4/mmm*) $a_p \times a_p \times 2a_p$ superstructure. Strontium and the rare earth ions are disordered over a single site, while the oxygen vacancies are localised on the apical O2 sites. Magnetisation measurements show that these materials undergo transitions to a spin-glass state at temperatures below 150 K, and that significant coupling occurs between the rare earth ions and the mixed $Co^{3+/4+}$ ions. Magnetisation measurements as a function of applied field reveals that below the transition temperature ferromagnetic ordering takes place at relatively large fields.

Keywords: strontium doped cobaltate, solid solution limits, perovskite superstructure, spin glass magnetism.

1. Introduction

There has been substantial recent interest in strontium-doped rare earth perovskites ($Ln_{1-x}Sr_xCoO_{3-\delta}$) as cathode materials for solid oxide fuels cells [1-4] and as high temperature ceramic membranes [5-6]. These phases also display novel magnetic behaviour, including glassiness [7-9] and room temperature ferromagnetism [10-15]. We have lately explored structural variation within the $Ln_{1-x}Sr_xCoO_{3-\delta}$ perovskite phase diagram and demonstrated that an extensive range of solid solution is present for the larger rare earth ions (La^{3+}, Pr^{3+}, Nd^{3+}, and Sm^{3+}) [16]. For Y^{3+} and the smaller lanthanide ions, the range of solid solution becomes increasingly restricted with decreasing ionic radii. Furthermore we have shown that a tetragonal superstructure is present for $Ln_{1-x}Sr_xCoO_{3-\delta}$ (Ln = Sm^{3+} - Yb^{3+}; $0.67 \leq x \leq 0.9$) with both cation and oxygen vacancy ordering. These phases show mixed $Co^{3+/4+}$ oxidation states with up to 50% Co(IV).

Our above study of demonstrated extended solid solution ranges beyond those previously observed for $Ln_{1-x}Sr_xCoO_{3-\delta}$ (Ln = La^{3+}, Pr^{3+} and Nd^{3+}), up to x = 0.90. While the lower boundaries (small x) of the $Ln_{1-x}Sr_xCoO_{3-\delta}$ phase diagram have been explored in some detail, it has become apparent that the upper boundaries have not been as clearly defined. This study explores the relationship between $Ln_{1-x}Sr_xCoO_{3-\delta}$ perovskite and trigonal $SrCoO_{3-\delta}$ structures as well as the magnetic properties of the former.

2. Samples and Methods

Synthesis

Polycrystalline samples of $Ln_{0.05}Sr_{0.95}CoO_{3-\delta}$ were prepared from spectroscopic grade powders of $SrCO_3$ (98+%), $Co(NO_3)_2.6H_2O$ (98%) and either Ln_2O_3 (*Ln* = La, Nd, Sm, Gd, Dy, Y, Er, Tm and Yb) (≥99.9%), Pr_6O_{11} (99.9%) or $Ho(NO_3)_3.5H_2O$ (99.9%). The powders were dissolved in dilute nitric acid and an intimate mixture of the metal oxides was formed via the decomposition of a citric acid-ethylene glycol sol-gel. The residues were pelleted and sintered in a tube furnace at 1100 °C under flowing oxygen for up to 3 days with intermediate re-grinding and re-pelleting until no further reaction was evident by powder X-ray diffraction. The samples were cooled from 1100 °C to room temperature at a rate of 2 °C per minute.

Thermogravimetry

Thermogravimetry of *ca.* 70 mg of each of the $Ln_{0.05}Sr_{0.95}CoO_{3-\delta}$ samples were carried out using a SETARAM TAG24 Simultaneous Thermogravimetric and Differential Thermal Analyser. The samples were reduced under a mixture of 3.5% hydrogen in nitrogen over a temperature range of 25 - 950 ° C at a heating rate of 5° C/minute. Each of the samples studied decomposed under hydrogen reduction to give the component oxides Ln_2O_3 and SrO as well as Co metal. As has been shown for other rare earth perovskite cobaltates [31], the observed mass loss is therefore apportioned to the change in oxygen content as Co^{n+} in the as–synthesised sample is reduced to Co metal.

Electron Diffraction

Electron diffraction (ED) was carried out using a Philips EM 430 Transmission Electron Microscope operating at 300 kV. Samples suitable for TEM work were prepared by the dispersion of finely ground material onto a holey carbon film.

Powder Diffraction Measurements

Powder X-ray diffraction measurements were made on a Scintag Inc. XGEN 4000 X-ray diffractometer at ambient temperature using Cu K_α radiation and a flat-plate sample holder. Data of sufficient quality for structural refinement were collected, over $5° < 2\theta < 105°$, in 0.02° steps, with 10 s acquisition times per step. Powder neutron diffraction data were collected on the MRPD instrument (λ = 1.6631 Å) at the HIFAR facility, Sydney, Australia. Structure refinements were carried out by the Rietveld method [32] using the RIETICA program [33] with pseudo-Voigt peak shapes and refined backgrounds.

Further details of the crystal structure investigations can be obtained from the Fachinformationszentrum Karlsruhe, 76344 Eggenstein-Leopoldshafen, Germany, (fax: +49 7247-808-66; email: mailto:crysdata@fiz-karlsruhe.de), quoting the depository number CDS-# for $Y_{0.05}Sr_{0.95}CoO_{3-\delta}$.

Magnetic Susceptibility

AC magnetic susceptibility was measured using a Lakeshore 7000 series AC susceptometer (School of Physics, University of New South Wales, Sydney, Australia) with a closed cycle helium refrigerator (CCR) (20 K < T < 320 K). Measurements were made in drift mode with a heater switched on manually when the sample reached room temperature. The maximum RMS magnetic field was 20 Oe and the AC frequency could be varied from 1 Hz to 10 kHz. Blank runs were performed to allow for the response of the sample holder.

DC magnetisation was measured using a Quantum Design MPMS-7 SQUID magnetometer (Institute for Superconducting and Electronic Materials, University of Wollongong, Australia) with a 7 T superconducting magnet, capable to temperatures from 4.2 K to 340 K.

3. Results and Discussion

The Structure of "$SrCoO_3$"

Stoichiometric $SrCoO_3$, containing only Co(IV) is not able to be produced via standard solid state synthesis under atmospheric conditions. $SrCoO_3$ has however been synthesised by Shaplygin and Lazercv in a high-pressure synthesis at 65 kbar using $KClO_4$ as an oxygen source [20]. Bezdicka and coworkers have also demonstrated that $Sr_2Co_2O_5$ can be oxidised to the perovskite $SrCoO_3$ via electrochemical methods [21]. A number of authors have investigated the phase relations in oxygen deficient $SrCoO_{3-\delta}$ and shown phases ranging from an orthorhombic, Brownmillerite structures [22] to hexagonal $BaNiO_3$-type structures [23, 24] and even perovskite-like cubic phases at elevated temperatures [25, 26]. Recently, Harrison and coworkers used powder neutron diffraction to show that the low-temperature hexagonal form of $SrCoO_{3-\delta}$ synthesised in air was actually a combination of trigonal $Sr_6Co_5O_{15}$ and a small amount of Co_3O_4 [27]. Our own attempts to synthesise $SrCoO_{3-\delta}$ under the same conditions as our $Ln_{1-x}Sr_xCoO_{3-\delta}$ phases also led to the formation of trigonal $Sr_6Co_5O_{15}$ and Co_3O_4.

Stabilisation of the Perovskite Phase

It was found that the perovskite phase could be stabilised by the introduction of a small amount (5%) of certain rare earth ions into the structure. Examination of $Ln_{0.05}Sr_{0.95}CoO_{3-\delta}$ compositions using powder X-ray diffraction reveal different phase behaviour depending on the ionic radius of the rare earth species. $La_{0.05}Sr_{0.95}CoO_{3-\delta}$ and $Pr_{0.05}Sr_{0.95}CoO_{3-\delta}$ (Figure 1a) form the same trigonal structure as $Sr_6Co_5O_{15}$ [27], while $Nd_{0.05}Sr_{0.95}CoO_{3-\delta}$ produces a mixture of both the $Sr_6Co_5O_{15}$ and perovskite structures. $Ln_{0.05}Sr_{0.95}CoO_{3-\delta}$ compositions containing rare earth ions smaller than Nd form phase-pure

perovskite structures. The XRD profile by way of example for $Y_{0.05}Sr_{0.95}CoO_{3-\delta}$ is shown in Figure 1(b). Attempts to form perovskite phases were unsuccessful for compositions more highly doped than x = 0.95. The composition $Y_{0.025}Sr_{0.975}CoO_{3-\delta}$ for example formed the trigonal "$Sr_6Co_5O_{15}$"-like structure.

These results add to our earlier work [16] that examined the $Ln_{1-x}Sr_xCoO_{3-\delta}$ perovskite phase diagram. Figure 2 shows the solid solution range for which perovskite structures form as a function of ionic radii. Compositions containing the larger lanthanide ions (La^{3+}, Pr^{3+}, Nd^{3+} and Sm^{3+}) show an extended solid solution range ($0 \leq x \leq 0.90$) and a number of structure types ranging from cubic to monoclinic. For perovskite phases containing lanthanide ions smaller than Sm^{3+}, the lower solid solution limit increases with decreasing ionic radii, while the upper limit is constant at 0.95. Thus, the solid solution range contracts from $0.4 \leq x \leq 0.95$ for *Ln* = Gd, to $0.90 \leq x \leq 0.95$ for *Ln* = Yb. In addition we have shown that a number of compositions crystallise with a modulated tetragonal (*I4/mmm*; $2a_p \times 2a_p \times 4a_p$) superstructure for $x > 0.6$ and for lanthanide ions smaller than Nd^{3+}.

Thermogravimetry

The overall oxygen content and average cobalt oxidation state for each single-phase sample was determined using thermogravimetric analysis (Table 1). It was found that the amount of oxygen vacancies (δ) in these $Ln_{0.05}Sr_{0.95}CoO_{3-\delta}$ phases varied between 0.19 and 0.22, leading to average cobalt oxidation states between 3.51+ and 3.56+.

The level of oxygen vacancies observed in this study are consistent with those previously observed for other $Ln_{1-x}Sr_xCoO_{3-\delta}$ (*Ln* = Y, Sm - Yb); $x > 0.60$) phases [16, 28]. These results confirm that there appears to be no systematic variation in oxygen content as a function of Sr doping levels. The average cobalt oxidation state on the other hand is heavily influenced by the amount of strontium present in the structure. The amount of Co^{4+} in these phases increases from 25% for $Ln_{0.33}Sr_{0.67}CoO_{3-\delta}$ [28] to 46% for $Ln_{0.10}Sr_{0.90}CoO_{3-\delta}$ [16] and up to 56% is observed in this study.

Electron Diffraction

Figure 3 shows (a) $<001>_p$, (b) $<110>_p$ and (c) $<111>_p$ zone axis selected area electron diffraction patterns (EDP's) of $Y_{0.05}Sr_{0.95}CoO_{2.79}$ which are typical of each of the smaller rare earth ion containing perovskite compounds. Note the presence of weak $\mathbf{G} \pm {}^1/_2<001>_p^*$ type satellite reflections in addition to the strong Bragg reflections of the underlying perovskite type average structure (labelled with the subscript p in Figure 3). The absence of $\mathbf{G} \pm {}^1/_2<110>_p^*$ type satellite reflections (particularly in the $<001>_p$ type zone axis EDP - Figure 3(a)) is strongly suggestive of an $a_p \times a_p \times 2a_p$ superstructure on the local scale. This is despite the fact that $\mathbf{G} \pm {}^1/_2<100>_p^*$ and $\mathbf{G} \pm {}^1/_2<010>_p^*$ type satellite reflections are invariably simultaneously observed in $<001>_p$ zone axis EDP's. This latter fact is attributed to fine scale twinning of the proposed $a_p \times a_p \times 2a_p$ superstructure.

X-ray Diffraction

Powder X-ray diffraction profiles for $Ln_{0.05}Sr_{0.95}CoO_{3-\delta}$ (Ln = Sm – Yb) were able to be indexed on a simple cubic (*Pm3m*; a ~ 3.846 Å). Careful examination of these profiles did not reveal any other superstructure peaks or additional splitting of the main perovskite diffraction lines. In particular, there was no evidence of the $a_p \times a_p \times 2a_p$ superstructure that was observed using electron diffraction.

The structure of each single-phase $Ln_{0.05}Sr_{0.95}CoO_{3-\delta}$ composition was refined based on a simple cubic perovskite cell. Each of the atoms were located at their typical high-symmetry positions, with Sr^{2+} and Ln^{3+} disordered over the *1b* (½,½,½) site. Refinement of the isotropic thermal parameters for each compound gave a very high value for the *3d* (½,0,0) oxygen site, suggesting substantial disorder between oxygen and vacancies. The refined unit cell parameters for the $Ln_{0.05}Sr_{0.95}CoO_{3-\delta}$ phases are listed in Table 1. The unit cell edges vary in the range 3.8459(1) Å to 3.8498(1) Å, although not in any systematic fashion with decreasing rare earth ionic radius. This is perhaps not surprising given the relatively small amount (5%) of rare earth ions in the structure. As has been previously noted for other $Ln_{1-x}Sr_xCoO_{3-\delta}$ compounds having the tetragonal (*I4/mmm*; $2a_p \times 2a_p \times 4a_p$) superstructure, the unit cell volume increases with Sr content; this being despite oxidation of Co^{3+} to the smaller Co^{4+} [16]. Comparison of the unit cell volumes for $Ln_{0.1}Sr_{0.9}CoO_{3-\delta}$ (Ln = Sm^{3+}, Gd^{3+}, Dy^{3+}, Y^{3+} and Ho^{3+}) (Table 3, ref. 16) with those in Table 1 for $Ln_{0.05}Sr_{0.95}CoO_{3-\delta}$, however do not show a consistent continuation of this trend. Refined unit cell volumes were found to be larger for x = 0.05 and Ln = Gd^{3+}, Y^{3+}, Er^{3+} and Yb^{3+} but smaller for Ln = Sm^{3+}, Dy^{3+}, Ho^{3+} and Tm^{3+}.

Neutron Diffraction

The powder neutron diffraction profile of $Y_{0.05}Sr_{0.95}CoO_{2.79}$ could not be indexed using a simple cubic (*Pm3m*) perovskite cell, but rather a tetragonal (*P4/mmm*) $a_p \times a_p \times 2a_p$ supercell was required. These data support our current electron diffraction results for this compound. The positions of each of the atoms were initially set at idealised values, with Y^{3+} and Sr^{2+} ions disordered over the *2h* (½,½,z) sites (z = ¼). All of the oxygen sites were set as being fully occupied. Early stages of the refinement did not place calculated intensity in any of the superstructure peaks. While most of the atoms occupied special sites within the structure, the location of Y1/Sr1 and O2 were allowed to move along the z-axis (Table 3). Independent refinement of the oxygen thermal parameters led to a significantly higher value at the O2 *2g* (0,0,z) site suggesting that significant oxygen vacancy disorder may be present. In the final stages of the refinement, the oxygen thermal parameters were constrained to be the same value, and the occupancy of the O2 site was allowed to vary. The refined O2 site occupancy of 0.81(1) is in very good agreement with that observed from thermogravimetric analysis. The observed, calculated and difference neutron powder diffraction profiles for $Y_{0.05}Sr_{0.95}CoO_{2.79}$ are shown in Figure 4; while the refined structure is shown in Figure 5. Structural parameters for $Y_{0.05}Sr_{0.95}CoO_{2.79}$ are listed in Table 2, refined atomic positions and thermal parameters are listed in Table 3 and refined bond lengths are listed in Table 4.

Oxidation of Co^{3+} to Co^{4+} is accompanied by a reduction in ionic radii from 0.61 Å to 0.53 Å (29). Given the average cobalt oxidation state of 3.54+, one would expect a cobalt oxygen bond length of 1.94 Å. The average refined cobalt-oxygen bond length at 1.918 Å was found to be slightly shorter, but still consistent with other compounds containing mixtures of Co(III) and Co(IV).

The average refined Y/Sr-O bond length of 2.715 Å is in very good agreement to that observed for other 12-fold coordinate strontium oxide compounds [29]. In contrast to other $Ln_{1-x}Sr_xCoO_{3-\delta}$ ($0.33 \leq x \leq 0.1$) compounds, we found no evidence from our neutron diffraction data to suggest ordering between Y^{3+} and the more than 15% larger Sr^{2+} ion. This is perhaps not such a surprise given that there is only one crystallographically distinct rare earth site in the structure, and relatively small amounts of Y^{3+}.

Magnetic Susceptibility

The real part of the AC magnetic susceptibility (χ') for $Ln_{0.05}Sr_{0.95}CoO_{3-\delta}$ (*Ln* = Y, Sm, Gd, Dy, Ho, Er, Tm and Yb) are shown in Figure 6(a). In each case, a magnetic transition is observed, with the observed transition temperatures listed in Table 5. Figure 6(a) shows a substantial variation in peak intensity and transition temperature for the different phases. Table 5 also lists the calculated effective moment (μ_{eff}) for the rare earth ions. While the peak intensity shows a general trend with the rare earth effective moment, the correlation is not perfect. Calculated effective moments listed in Table 5 have magnitudes in the order $Dy^{3+} > Ho^{3+} > Er^{3+} > Gd^{3+} > Tm^{3+} > Yb^{3+} > Sm^{3+} > Y^{3+}$, while the peak intensities shown in Figure 6(a) are $Ho^{3+} > Dy^{3+} > Sm^{3+} > Yb^{3+} > Gd^{3+} > Tm^{3+} > Er^{3+} > Y^{3+}$. Transition temperatures for the $Ln_{0.05}Sr_{0.95}CoO_{3-\delta}$ phases on the other hand show the order $Sm^{3+} > Dy^{3+} > Gd^{3+} > Yb^{3+} > Ho^{3+} > Tm^{3+} > Er^{3+} > Y^{3+}$.

The percentage of Co^{4+} present in these compounds varies slightly from 51% in the Tm phase to 56% in the Ho phase (Table 5). Comparison of the relatively low peak intensity and low transition temperature for $Y_{0.05}Sr_{0.95}CoO_{2.79}$ compared with the other rare earth phases clearly demonstrates the importance of coupling between the cobalt and rare earth moments. Figure 6(b) shows a comparison between the AC susceptibility data for $Y_{0.05}Sr_{0.95}CoO_{2.79}$ (×) and $Y_{0.10}Sr_{0.90}CoO_{2.77}$ (◊) (following our earlier study, ref. 16). The substantially higher intensity of the magnetic peak centred at ~100 K for the x = 0.95 phase as compared to the x = 0.90 phase is a direct reflection of the higher Co^{4+} content (54% for $Y_{0.05}Sr_{0.95}CoO_{2.79}$ as opposed to 45% for $Y_{0.10}Sr_{0.90}CoO_{2.77}$).

DC magnetisation measurements were also conducted on $Y_{0.05}Sr_{0.95}CoO_{2.79}$. Figure 7 shows the zero-field cooled (ZFC) and field cooled (FC) molar susceptibility (χ_M) of $Y_{0.05}Sr_{0.95}CoO_{2.79}$ as a function of temperature under a 50 Oe DC magnetic field. The two curves diverge at ~125 K with the ZFC data (filled, black squares) having a maximum at ~102 K and then tending towards a low value of susceptibility (< 0.07 emu/mol) at 5 K. In contrast, the FC data (open circles) undergoes a maximum at 80 K and saturates to a constant 0.53 emu/mol at temperatures less than 10 K. This behaviour is consistent with the formation of a spin-glass at low temperatures.

The DC molar susceptibility (χ_M) of $Y_{0.05}Sr_{0.95}CoO_{2.79}$ was also measured at 1 T; this data being displayed as $1/\chi_M$ versus temperature in Figure 8. The linear region of this curve indicates that for high temperatures (> 200 K) $Y_{0.05}Sr_{0.95}CoO_{2.79}$ obeys the Curie-Weiss law ($\chi_M = C_M/(T-\theta)$). These data were fitted to the Curie-Weiss law for 240 K ≤ T ≤ 340 K, leading to values of the Curie constant (C_M) of 1.027 emu K/mol and the Weiss parameter (θ) of 171 K. The positive value of the Weiss parameter reveals that ferromagnetic interactions are present in this compound. As cobalt ions are the only species present with unpaired valence electrons, the Curie constant could be used to determine an effective moment (μ_{eff}) per cobalt ion of 2.87 B.M. Given the spin-only moments for low-spin (LS), intermediate spin (IS) and high-spin (HS) Co^{3+} and Co^{4+} (Table 5), and the fact that a combination of 46% Co^{3+} and 54% Co^{4+} is present in $Y_{0.05}Sr_{0.95}CoO_{2.79}$, one might expect an effective moment per mole of compound ranging from 1.27 B.M to 5.47 B.M. The combination of low-spin Co^{3+}

and intermediate-spin Co^{4+} gives very good agreement (2.84 B.M.) with our observed effective moment.

Our observed magnetic behaviour of $Ln_{0.05}Sr_{0.95}CoO_{3-\delta}$ is consistent with that previously observed for other strontium-doped rare earth cobaltates. Wu and Leighton [31] have examined in detail the magnetic behaviour of $La_{1-x}Sr_xCoO_{3-\delta}$ over an extended range of solid solution ($0 \leq x \leq 0.7$), which they broadly characterise as a "glassy ferromagnet". For $x > 0.2$, they suggested that the magnetism was the results of the coalescence of short-range-ordered ferromagnetic clusters. Fitting of their DC susceptibility data above the Curie temperature suggest that both Co^{3+} and Co^{4+} were in intermediate spin states.

The response of the magnetism of $Y_{0.05}Sr_{0.95}CoO_{2.79}$ to both temperature and field is apparent by examination of Figure 9(a)-(c). Above the transition temperature, a typical linear paramagnetic response is observed (as shown in Figure 9(a) at 300 K). At 75 K, just below the transition temperature, the magnetisation shows saturation behaviour at high fields indicative of ordering of ferromagnetic domains (Figure 9(b)). At the lowest temperature measured (5 K) the magnetisation shows a combination of hysteresis as well as saturation at high applied fields (Figure 9(c)).

Conclusions

We have studied the stability of very highly Sr-doped compounds $Ln_{0.05}Sr_{0.95}CoO_{3-\delta}$ as a function of different rare earth radii and shown that phase-pure perovskite structures are stabilised for rare ions smaller than Nd^{3+}. A combination of X-ray, electron and neutron diffraction has revealed a tetragonal (*P4/mmm*) $a_p \times a_p \times 2a_p$ superstructure with Ln^{3+} and Sr^{2+} ions disordered over a single crystallographic site. The oxygen vacancies within the structure appear to be localised at the (0,0,z) sites. AC and DC magnetisation measurements show that these materials undergo transitions at approximately 100 K to a spin glass state with evidence of coupling between the mixed $Co^{3+/4+}$ and rare earth ions. At relatively large applied magnetic fields these compounds undergo ordering to a ferromagnetic state.

Acknowledgments

RLW and MJ acknowledge the Australian Research Council (ARC) for financial support in the form of ARC Discovery Grants.

References

1. S. J. Skinner, *International Journal of Inorganic Materials* 3, 113 (2001).

2. H. Y. Tu, Y. Takeda, N. Imanishi and O. Yamamoto, *Solid State Ionics* **100**, 283 (1997).

3. R. H. E. van Doorn and A. J. Burggraaf, *Solid State Ionics* **128**, 65 (2000).

4. S. B. Adler, *Solid State Ionics* **111**, 111 (1998).

5. A. V. Kovalevsky, V. V. Kharton, V. N. Tikhonovich, E. N. Naumovich, A.A.Tonoyan, O. P. Reut and L. S. Boginsky, *Materials Science and Engineering* B**52**, 105 (1998).

6. V. V. Kharton, A. A. Yaremchenko, A. V. Kovalevsky, A. P. Viskup, E.N.Naumovich, and P. F. Kerko, *J. Membrane Sci.* **163**, 307 (1999).

7. S. Mukherjee, R. Ranganathan, P.S. Anikumar and P. A. Joy, *Phys. Rev. B* **54**, 9367 (1996).

8. P.S. Anil Kumar, P. A. Joy and S. K. Date, *J. Phys.: Condens. Matter* **10**, L487 (1998).

9. D. N. H. Nam, K. Jonason, P. Nordblad, N. V. Khiem and N. X. Phuc, *Phys. Rev. B* **59**, 4189 (1998).

10. K. Asai, O. Yokokura, N. Nishimori, H. Chou, J. M. Tranquada, G. Shirane, S.Higuchi, Y. Okajima and K. Kohn, *Phys. Rev. B* **50**, 3025 (1994).

11. M. A. Senaris-Rodriguez and J. B. Goodenough, *J. Solid State Chem.* **118**, 323 (1995).

12. R. Caciuffo, D. Rinaldi, G. Barucca, J. Mira, J. Rivas, M. A. Senaris Rodriguez, P.G.Radaelli, D. Fiorani and J. B. Goodenough, *Phys. Rev. B* **59**, 1068 (1999).

13. J. Mira, J. Rivas, M. Vazquez, J. M. Garcia-Beneytez, J. Arcas, R. D. Sanchez and M.A. Senaris-Rodriguez, *Phys. Rev. B* **59**, 123 (1999).

14. R. Ganguly, I. K. Gopalakrishnan and J. V. Yakhmi, *Physica B* **271**, 116 (1999).

15. Sujeet Chaudhary, S. B. Roy and P. Chaddah, *J. Alloys and Compounds* **326**, 112 (2001).

16. M. James, D. Cassidy, D. J. Goossens and R. L. Withers, *J. Solid State Chem.* , In Press (2003).

17. M.Karpinnen, M.Matvejeff, K.Salomaeki and H.Yamauchi, *J. Materials Chem.* **12**, 1761 (2002).

18. H. M. Rietveld, *J. Appl. Crystallogr.* **2**, 65 (1969).

19. B. A. Hunter, 'Rietica – A Visual Rietveld Program" in Commission on Powder Diffraction Newsletter, 20, p. 21 (1998).
Available at: http://www.iucr.org/iucr-top/comm/cpd/Newsletters/

20. I. S. Shaplygin and V. B. Lazercv, *Russ. J. Inorg. Chem. Engl. Transl.* **30,** 3214 (1985).

21. P. Bezdicka, A. Wattiaux, J. C. Grenier, M. Pouchard and P. Hagenmuller, *Z. Anorg. Allg. Chem.* **619**, 7 (1993).

22. Y. Ito, R. F. Klie, N. D. Browning and T. J. Mazanec, *J. Am. Ceram. Soc.* **85**, 969 (2002).

23. Y. Takea, R. Kanno, T. Takeda, O. Yamamoto, M. Takano and Y. Bando, *Z. Anorg. Allg. Chem.* **540-541**, 259 (1986).
24. P. D. Battle, T. C. Gibb and A. T. Steel, *J. Chem. Soc., Dalton Trans.* 2359 (1987).
25. J. Rodriguez, J. M. Gonzalez-Calbet, J. C. Grenier, J. Pannetier and M. Anne, *Solid State Commun.* **62**, 231 (1987).
26. V. V. Vashook, M. V. Zinkevich and Yu. G. Zonov, *Solid State Ionics*, **116** , 129 (1999).
27. W. T. A. Harrison, S. L. Hegwood and A. J. Jacobson, *J. Chem. Soc. Chem. Commun.*, 1953-1954 (1995).
28. R. L. Withers, M. James and D. J. Goossens, *J. Solid State Chem.*, **174(1)** 198 -208 (2003).
29. R. D. Shannon, *Acta Cryst.* **A32**, 751 (1976).
30. D. J. Goossens, K. F. Wilson, M. James, A. J. Studer and X. L. Wang, *Phys. Rev. B*, Submitted (2003).
31. J. Wu and C. Leighton, *Phys. Rev. B*, **67**, 174408 (2003).

Table 1. Number of Oxygen Vacancies, Average Cobalt Oxidation State and Refined Simple Perovskite Unit Cell Parameters for $Ln_{0.05}Sr_{0.95}CoO_{3-\delta}$ (Ln = Sm – Yb).

	δ	**% Co^{4+}**	***a* (Å)**	***V* (Å^3)**
$Sm_{0.05}Sr_{0.95}CoO_{3-\delta}$	0.20	55	3.8468(1)	56.924(2)
$Gd_{0.05}Sr_{0.95}CoO_{3-\delta}$	0.22	52	3.8498(1)	57.059(2)
$Dy_{0.05}Sr_{0.95}CoO_{3-\delta}$	0.21	54	3.8463(1)	56.902(2)
$Y_{0.05}Sr_{0.95}CoO_{3-\delta}$	0.21	54	3.8486(1)	57.002(1)
$Ho_{0.05}Sr_{0.95}CoO_{3-\delta}$	0.19	56	3.8459(1)	56.886(1)
$Er_{0.05}Sr_{0.95}CoO_{3-\delta}$	0.20	55	3.8473(1)	56.947(2)
$Tm_{0.05}Sr_{0.95}CoO_{3-\delta}$	0.22	51	3.8479(1)	56.974(2)
$Yb_{0.05}Sr_{0.95}CoO_{3-\delta}$	0.21	54	3.8464(1)	56.906(2)

Table 2. Structural Parameters for $Y_{0.05}Sr_{0.95}CoO_{2.79}$, refined from Powder Neutron Diffraction Data.

Formula	$Y_{0.05}Sr_{0.95}CoO_{2.79}$
Mass	191.258
Space Group	*P4/mmm*
Z	2
a (Å)	3.8338(4)
c (Å)	7.6845(4)
V (Å^3)	112.95(2)
ρ_{calc} (g cm^{-3})	5.624
No. of Reflections	73
R_P; R_{WP}; R_B	1.57; 2.14; 0.80

Table 3. Refined Atomic Positions and Thermal Parameters (B_{iso}; Å^2×100) for $Y_{0.05}Sr_{0.95}CoO_{2.79}$.

Atom	**Site**	**x**	**y**	**z**	**B_{iso}**	**Occ.**
Co1	*1a*	0	0	0	0.4(1)	1
Co2	*1b*	0	0	½	0.4(1)	1
Y1/Sr1	*2h*	½	½	0.2370(4)	0.9(1)	0.05/0.95
O1	*2f*	½	0	0	2.0(1)	1
O2	*2g*	0	0	0.2530(6)	2.0(1)	0.81(1)
O3	*2e*	½	0	½	2.0(1)	1

Table 4. Refined Bond Lengths (Å)

Co1 - O1 (× 4)	1.917(1)
Co1 – O2 (× 2)	1.944(5)
Co2 – O2 (× 2)	1.898(5)
Co2 – O3 (× 4)	1.917(1)
Average Co - O	1.918
Y1/Sr1 – O1 (× 4)	2.644(2)
Y1/Sr1 – O2 (× 4)	2.714(1)
Y1/Sr1 – O3 (× 4)	2.786(2)
Average Y/Sr - O	2.715

Table 5. Magnetic Ordering Temperatures (T_c (K)) for $Ln_{0.05}Sr_{0.95}CoO_{3-\delta}$, Ground State Configurations and Effective Ionic Moments (μ_{eff} (B.M.)).

	T_c (K)	**Unpaired Electrons**	**μ_{eff} (B.M.)[a]**	**% Co^{4+} [b]**
Co^{3+}		$3d^6$		
Low Spin		0 ($e_g^0 t_{2g}^6$)	0	
Intermediate Spin		2 ($e_g^1 t_{2g}^5$)	2.83	
High Spin		4 ($e_g^2 t_{2g}^4$)	4.90	
Co^{4+}		$3d^5$		
Low Spin		1 ($e_g^0 t_{2g}^5$)	1.73	
Intermediate Spin		3 ($e_g^1 t_{2g}^4$)	3.87	
High Spin		5 ($e_g^2 t_{2g}^3$)	5.92	
Y	99	0	0	54
Sm	148	5 ($4f^5$)	0.85	55
Gd	127	7 ($4f^7$)	7.94	52
Dy	129	5 ($4f^9$)	10.65	54
Ho	122	4 ($4f^{10}$)	10.60	56
Er	106	3 ($4f^{11}$)	9.58	55
Tm	108	2 ($4f^{12}$)	7.56	51
Yb	126	1 ($4f^{13}$)	4.54	54

[a] $\mu_{eff} = g[J(J+1)]^{½}$; $g = 3/2 + [S(S+1) – L(L+1)] / 2J(J+1)$

[b] From thermogravimetric measurements (Table 1).

Figure Captions

Figure 1. X-ray diffraction profiles for **(a)** $Pr_{0.05}Sr_{0.95}CoO_{3-\delta}$ and **(b)** $Y_{0.05}Sr_{0.95}CoO_{3-\delta}$. showing trigonal and perovskite structures respectively.

Figure 2. The $Ln_{1-x}Sr_xCoO_{3-\delta}$ perovskite phase diagram. Compositions having the metrically tetragonal (*P4/mmm*; $a_p \times a_p \times 2a_p$) superstructure are shown by crosses (+), while those having the metrically tetragonal (*I4/mmm*; $2a_p \times 2a_p \times 4a_p$) superstructure are indicated by ×. Compositions having rhombohedral structures are indicated by ♦. Simple cubic structures are indicated by •. Metrically cubic structures with orientational twinning of a local tetragonal ($a_p \times a_p \times 2a_p$) superstructure are indicated by (◊). Orthorhombic structures are indicated by ▲.

Figure 3(a) $<001>_p$, **(b)** $<110>_p$ and **(c)** $<111>_p$ zone axis selected area electron diffraction patterns (EDP's) for $Y_{0.05}Sr_{0.95}CoO_{2.79}$.

Figure 4. The observed (+), calculated and difference neutron diffraction profiles for $Y_{0.05}Sr_{0.95}CoO_{2.79}$.

Figure 5. The refined structure of $Y_{0.05}Sr_{0.95}CoO_{2.79}$. The O2 sites at (0, 0, ~¼) also contain oxygen vacancies, while both Y and Sr are disordered over the Y1/Sr1 sites at (½,½, ~¼).

Figure 6. The real part (χ') of the AC magnetic susceptibility versus temperature of $Ln_{0.05}Sr_{0.95}CoO_{3-\delta}$ (Ln = Y, Sm – Yb).

Figure 6(b). Comparison between the AC susceptibility data for $Y_{0.05}Sr_{0.95}CoO_{2.79}$ (×) and $Y_{0.10}Sr_{0.90}CoO_{2.77}$ (◊).

Figure 7. The zero-field cooled (ZFC) (black squares) and field cooled (FC) (open circles) molar susceptibility (χ_M) of $Y_{0.05}Sr_{0.95}CoO_{2.79}$ versus temperature under a 50 Oe DC magnetic field.

Figure 8. The inverse DC molar susceptibility ($1/\chi_M$) of $Y_{0.05}Sr_{0.95}CoO_{2.79}$ versus temperature under an applied field of 1 T.

Figure 9. The magnetisation (M) versus applied magnetic field (H) curves for $Y_{0.05}Sr_{0.95}CoO_{2.79}$ **(a)** at 300 K (open triangles); **(b)** at 75 K (open circles) and **(c)** at 5 K (closed circles).

Figure 1(a)

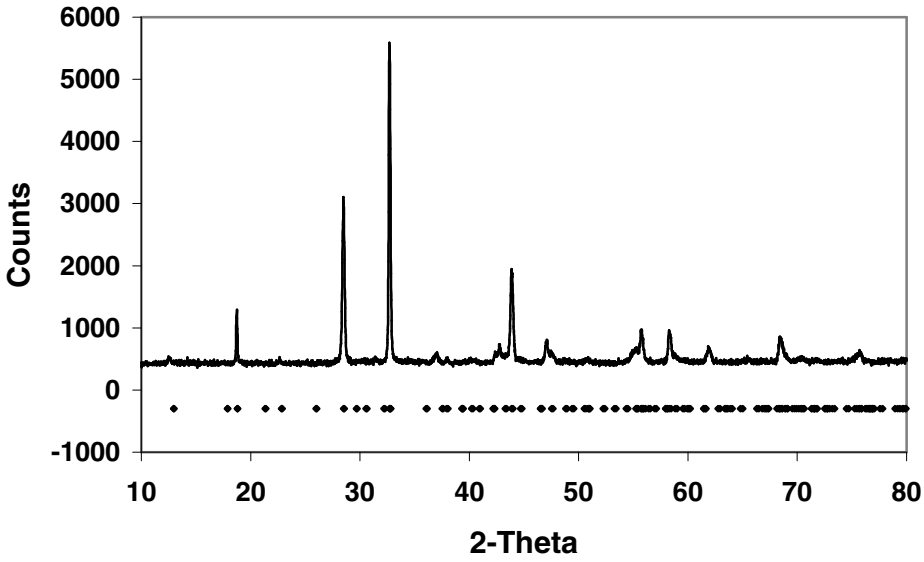

Figure 1(b)

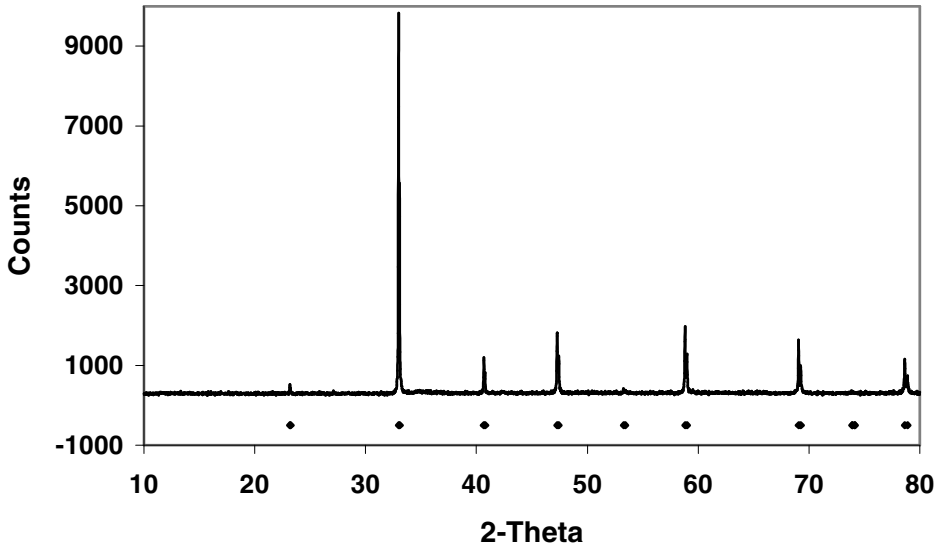

Figure 2.

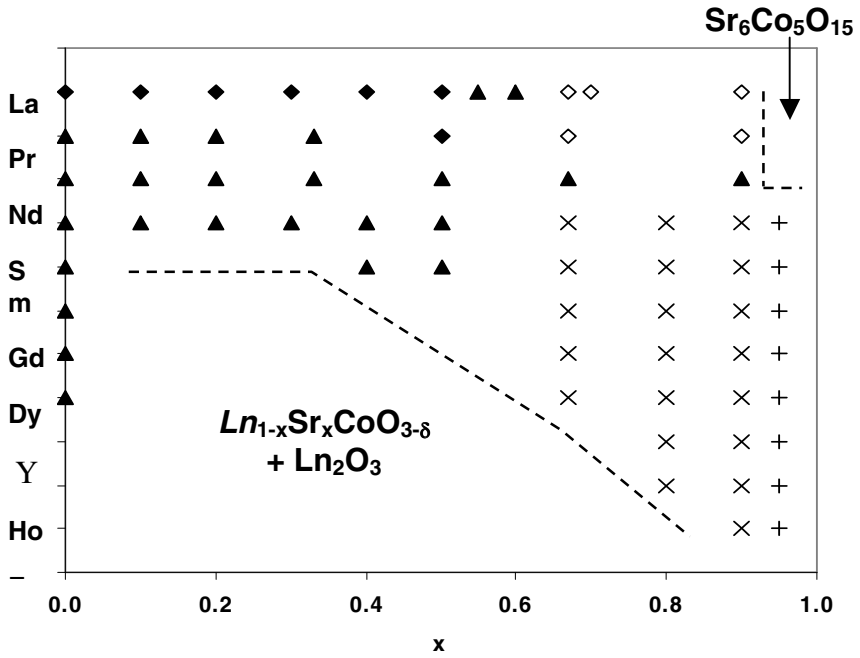

Figure 3(a)

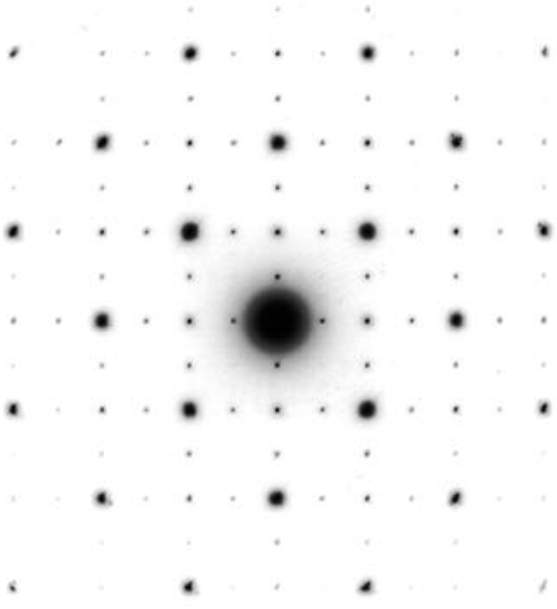

Figure 3(b)

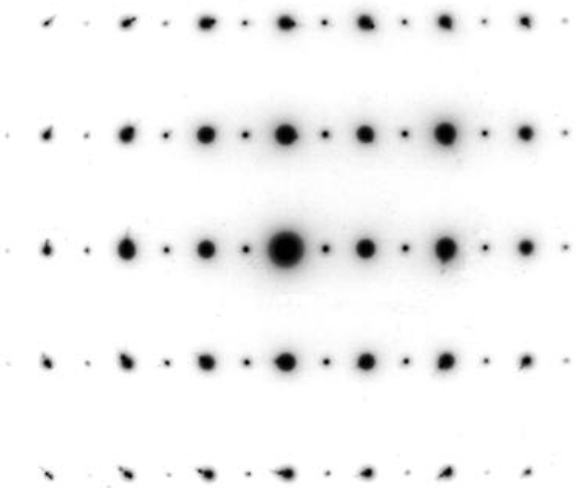

Figure 3(c)

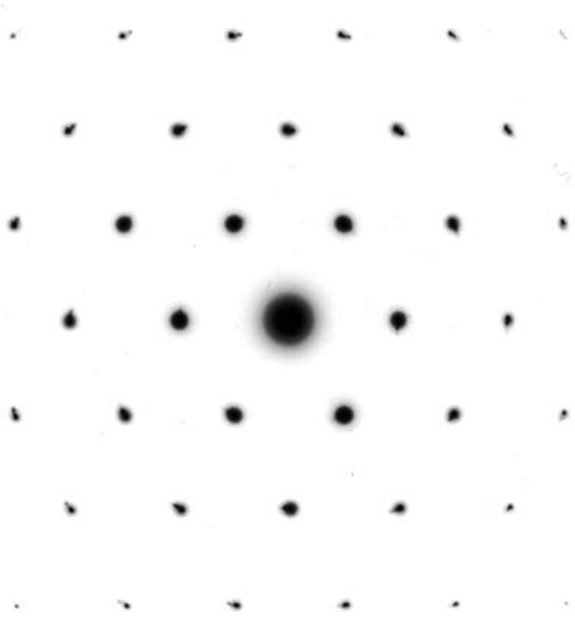

Figure 4.

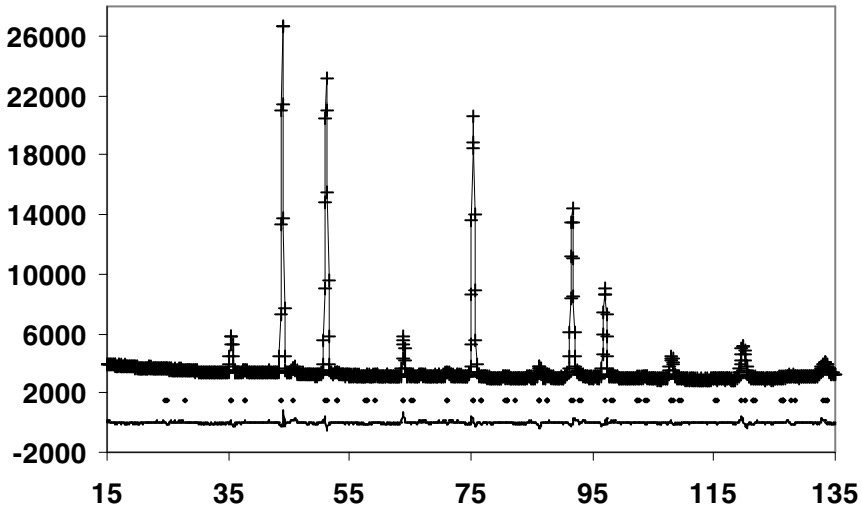
26000
22000
18000
14000
10000
6000
2000
-2000
15
35
55
75
95
115
135

Figure 5.

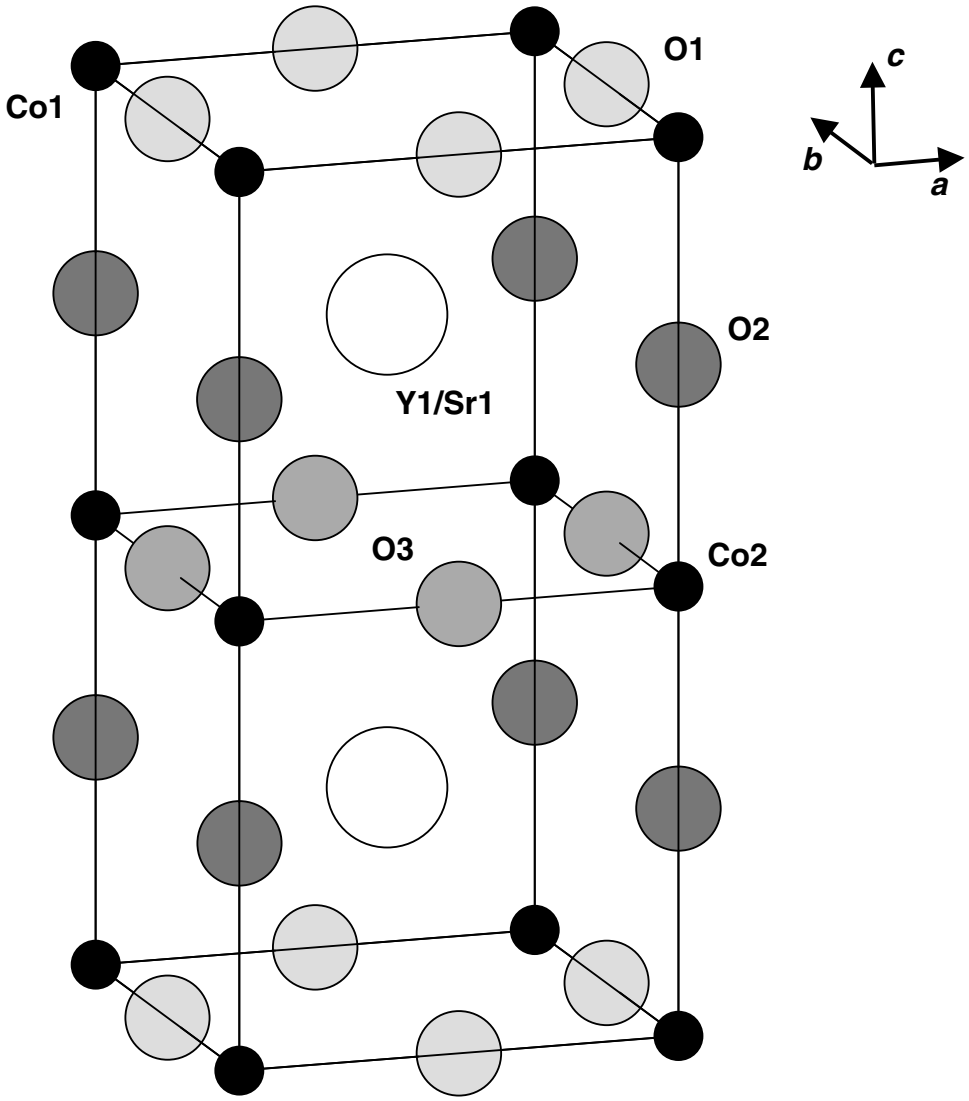

Figure 6(a).

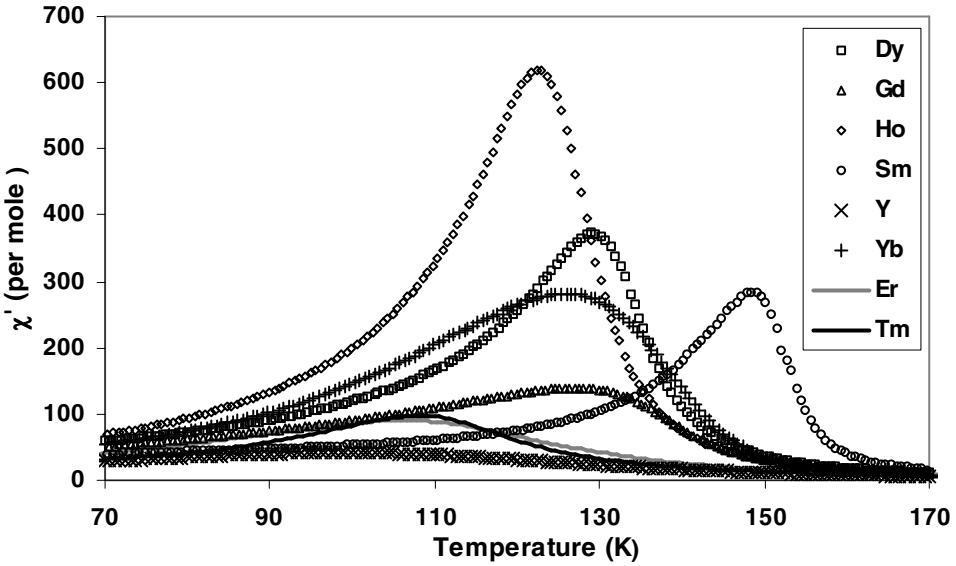

Figure 6(b).

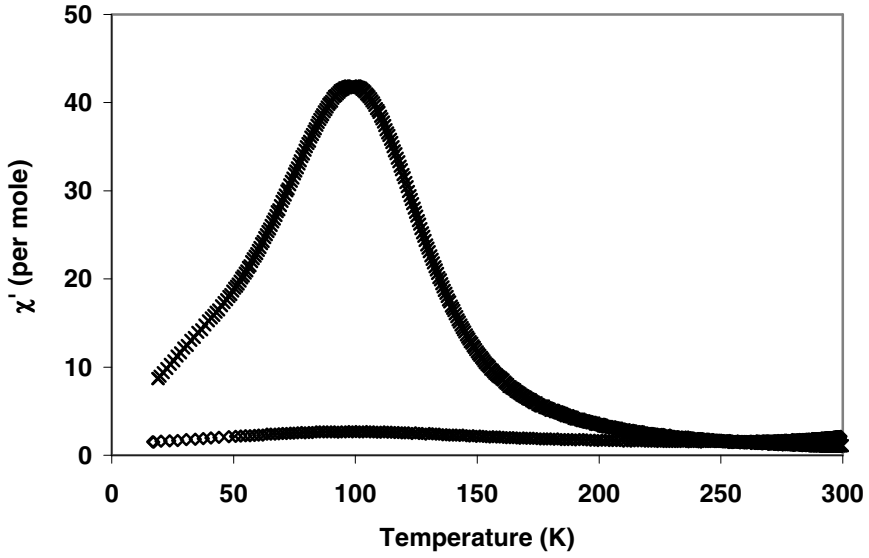

Figure 7.

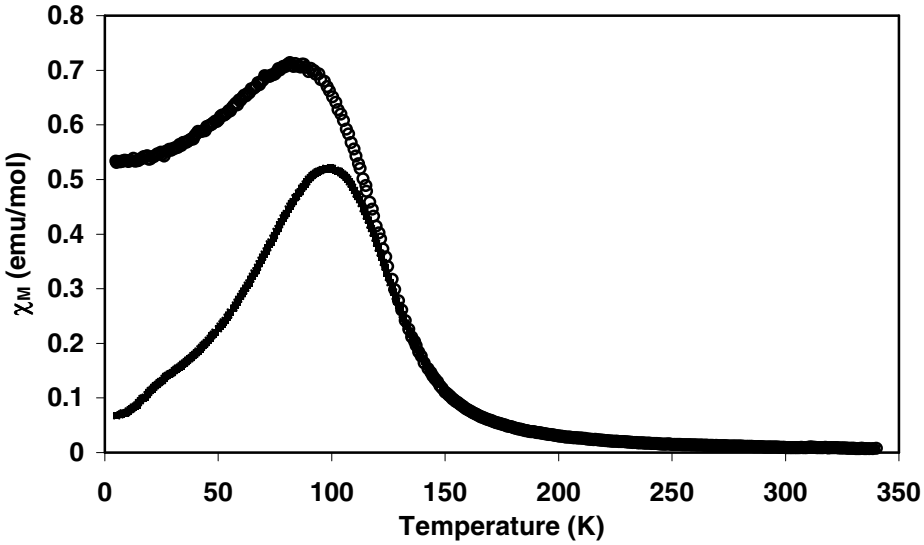

Figure 8.

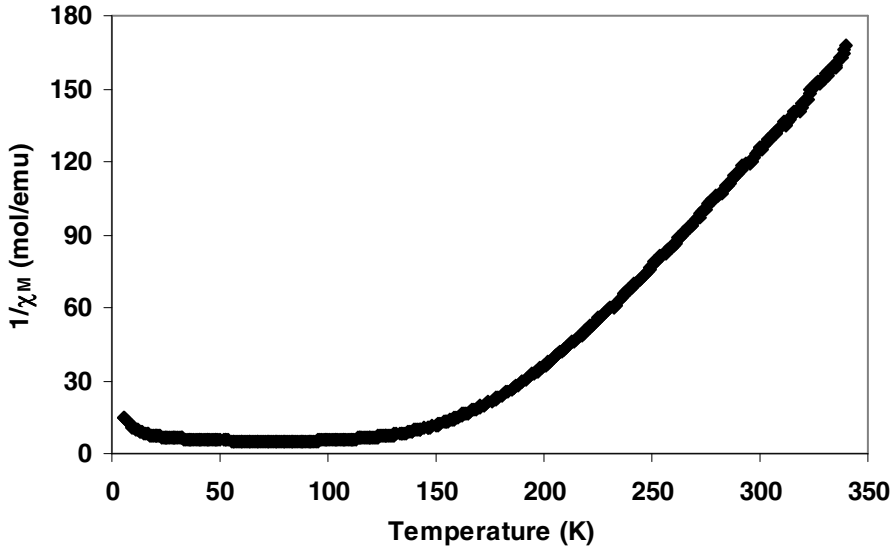

Figure 9(a).

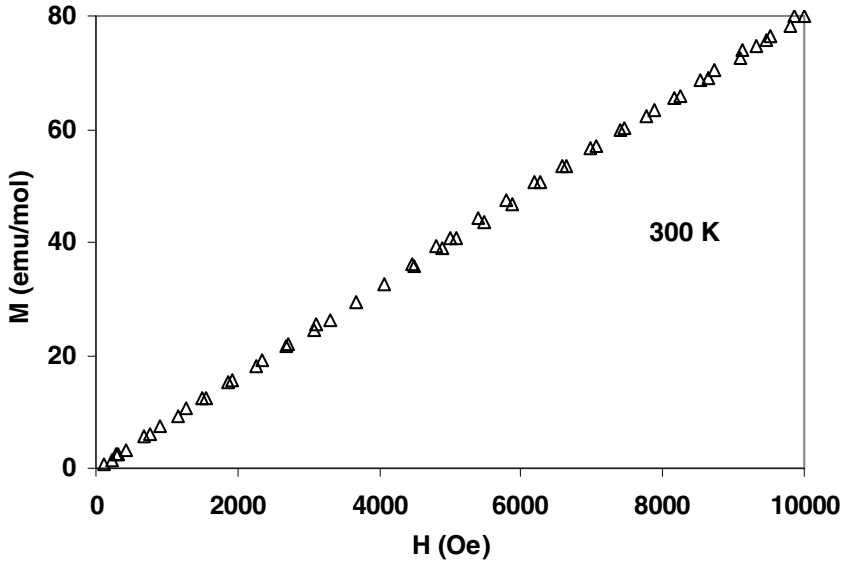

Figure 9(b).

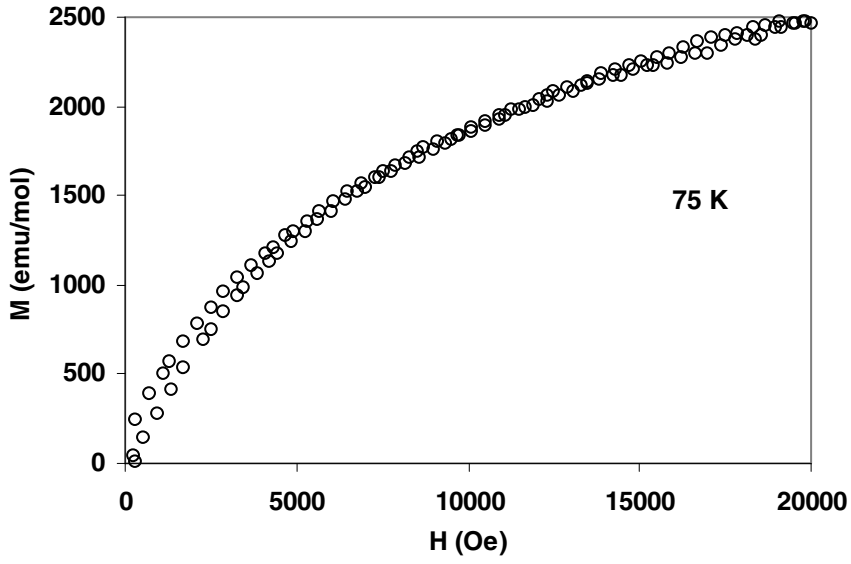

Figure 9(c).

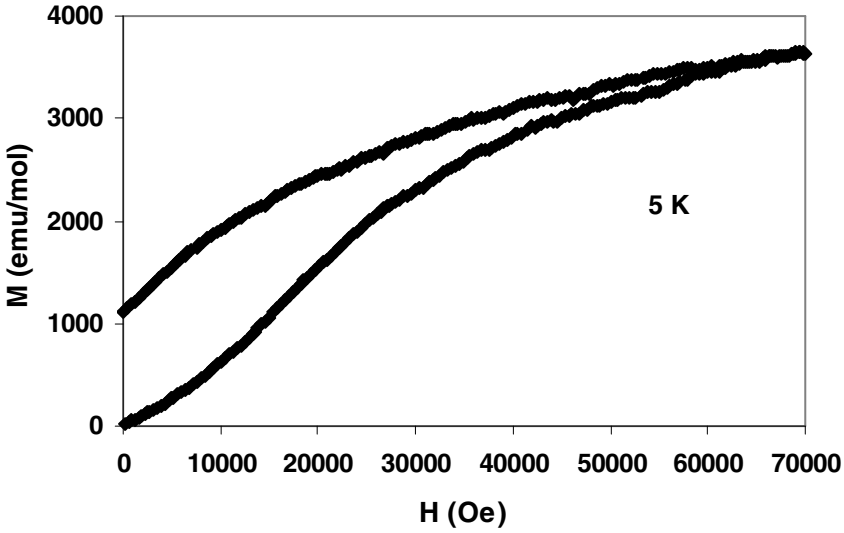
4000
3000
2000
1000
0
M (emu/mol)
5 K
0
10000
20000
30000
40000
50000
60000
70000
H (Oe)